Compressed Sensing Microscopy with Scanning Line Probes

Anonymous Author(s)
Affiliation
Address
`email`

Abstract

In applications of scanning probe microscopy, images are acquired by raster scanning a point probe across a sample. Viewed from the perspective of compressed sensing (CS), this pointwise sampling scheme is inefficient, especially when the target image is structured. While replacing point measurements with delocalized, incoherent measurements has the potential to yield order-of-magnitude improvements in scan time, implementing the delocalized measurements of CS theory is challenging. In this paper we study a partially delocalized probe construction, in which the point probe is replaced with a continuous line, creating a sensor which essentially acquires line integrals of the target image. We show through simulations, rudimentary theoretical analysis, and experiments, that these line measurements can image sparse samples far more efficiently than traditional point measurements, provided the local features in the sample are enough separated. Despite this promise, practical reconstruction from line measurements poses additional difficulties: the measurements are partially coherent, and real measurements exhibit nonidealities. We show how to overcome these limitations using natural strategies (reweighting to cope with coherence, blind calibration for nonidealities), culminating in an end-to-end demonstration.

1 Introduction

Scanning probe microscopy (SPM) is a fundamental technique for imaging interactions between a probe and the sample of interest. Unlike traditional optical microscopy, the resolution achievable by SPM is not constrained by the diffraction limit, making SPM especially advantageous for nanoscale, or atomic level imaging, which has widespread applications in chemistry, biology and materials science [1]. Conventional implementations of SPM typically adopt a raster scanning strategy, which utilizes a probe with small and sharp tip, to form a pixelated heatmap image via point-by-point measurements from interactions between the probe tip and the surface. Despite their capability of nanoscale imaging, SPM with pointwise measurement is inherently slow, especially when scanning a large area or producing high-resolution images.

When the target signal is highly structured, compressed sensing (CS) [2, 3, 4] suggests it is possible to design a data acquisition scheme in which the number of measurements is largely dependent on the signal complexity, instead of the signal size, from which the signal can be efficiently reconstructed algorithmically. In nanoscale microscopy, images are often spatially sparse and structured. CS theory suggests for such signals, localized measurements such as pointwise samples are inefficient. In contrast, delocalized, spatially spread measurements are better suited for reconstructing a sparse image.

Unfortunately, the dense (delocalized) sensing schemes suggested by CS theory (and used in other applications, e.g., [5, 6, 7]) are challenging to implement in the setting of micro/nanoscale imaging. Motivated by these concerns, [8] introduced a new type of *semilocalized* probe, known as a *line probe*, which integrates the signal intensity along a straight line, and studied it in the context of a particular microscopy modality known as scanning electrochemical microscopy (SECM) [9, 10]. In SECM with *line*

Figure 1: Left: lab made SECM device with line probe. Right: closeup side view of line probe near a sample surface.

probe, the working end of the probe constitutes a straight line, produces a single measurement by collecting accumulated redox reaction current induced by the probe and sample. These line measurements are semilocalized, samples a spatially sparse image more efficiently than measurements from point probes, and "has an edge" on high resolution imaging since a thin and sharp line probe can be manufactured with ease. Moreover, experiments in [8] suggest that a combination of line probes and compressed sensing reconstruction could potentially yield order-of-magnitude reductions in imaging time for sparse samples.
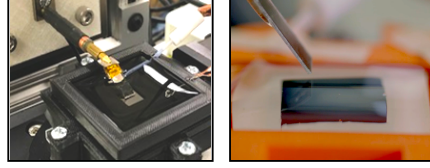
Realizing the promise of line probes (both in SECM and in microscopy in general) demands a more careful study of the mathematical and algorithmic problems of image reconstruction from line scans. Because these measurements are structured, they deviate significantly from conventional CS theory, and basic questions such as the number of line scans required for accurate reconstruction are currently unanswered. Moreover, practical reconstruction from line scans requires modifications to accommodate nonidealities in the sensing system. In this paper, we will address both of these questions through rudimentary analysis and experiments, showing that if the local features are either small or separated, then stable image reconstruction from line scans is attainable.

1.1 Related work

Compressed sensing tomography. Line measurements also arise in *computational tomography* (CT) imaging [11, 12, 13, 14, 15, 16]. Classical CT reconstruction recovers an image from densely sampled line scans, by approximately solving an inverse problem [17, 18]. These methods do not incorporate the prior knowledge of the structure of the target image, and degrade sharply when only a few CT scans are available. Compressed sensing offers an attractive means of reducing the number of measurements needed for accurate CT image reconstruction, and has been employed in applications ranging from medical imaging to (cryogenic) electron transmission microscopy [19, 20, 21, 22, 23, 24, 25, 26]. The dominant approach assumes that the target image is sparse in a Fourier or wavelet basis, and reconstructs it via ℓ^1 minimization or related techniques. Images in SECM and related modalities typically exhibit much stronger structure: they often consist some number of small particles [27, 28], or other repeated motifs [29]. In this situation, CS is especially promising. On the other hand, as we will see below, understanding the interaction between line scans and spatially localized features demands that we move beyond conventional CS theory.

Mathematical theory of line scans: Radon transform and image super-resolution. The question of recoverability from line measurements is related to the theory of the *Radon transform*, which corresponds to a limiting situation in which line scans at every angle are available [30, 31, 32]. The Radon transform is invertible, meaning perfect reconstruction is possible (albeit not stable) in this limiting situation. Due to the *projection slice theorem* [33], the line projections are inherently lowpass, and so the line scan reconstruction problem is related to superresolution imaging [34]. When the image of interest consists of sparse point sources, the image can be stably recovered from its low-frequency components, provided the point sources are sufficiently separated [35]. Similarly, we can hope to achieve stable recovery of localized features from line scans as long as the features are sufficiently separated.

2 Line measurement model

To implement line scans for SECM, a line probe (Figure 1) is mounted on an automated arm which positions the probe onto the sample surface. The line scan signal is generated by placing this line probe in different places, and measuring the integrated current induced by the interaction between the line probe and the electroactive part of the sample. In a pragmatic
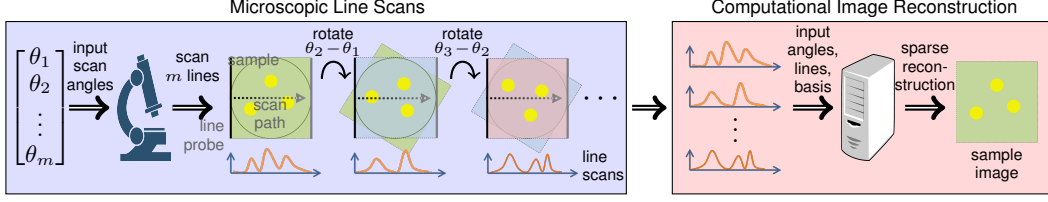
Figure 2: Flow chart for scanning procedure of SECM with continuous line electrode probe.

scanning procedure (Figure 2), the user will choose distinct scanning angles $\theta_1, \ldots, \theta_m$. For each angle θ, the line probe is oriented in direction $\boldsymbol{u}_\theta = (\cos\theta, \sin\theta)$ and swept along the normal direction $\boldsymbol{u}_\theta^\perp = (\sin\theta, -\cos\theta)$. Each sweep of probe generates the projection of the target image along the probe direction $\boldsymbol{u}_\theta$; collecting these projections for each θ_i, we obtain our complete set of measurements.

Line projection. To describe the scanning procedure more precisely, we begin with a mathematical idealization, in which the probe measures a line integral of the image. In this model, when the probe body is oriented in direction $\boldsymbol{u}_\theta$ at position t, we observe the integral of the image over $\ell_{\theta, t} := \{\boldsymbol{w} \in \mathbb{R}^2 \mid \langle \boldsymbol{u}_\theta^\perp, \boldsymbol{w} \rangle = t\}$:

$$\mathcal{L}_\theta[\boldsymbol{Y}](t) := \int_{\ell_{\theta, t}} \boldsymbol{Y}(\boldsymbol{w}) \, d\boldsymbol{w} := \int_s \boldsymbol{Y}\left(s \cdot \boldsymbol{u}_\theta + t \cdot \boldsymbol{u}_\theta^\perp\right) \, ds. \tag{2.1}$$

Collecting these measurements for all t, we obtain a function $\mathcal{L}_\theta[\boldsymbol{Y}]$ which is the projection of the image along the direction $\boldsymbol{u}_\theta$. We refer to the operation $\mathcal{L}_\theta : L^2(\mathbb{R}^2) \to L^2(\mathbb{R})$ as a *line projection*. Combining projections in m directions $\Theta = \{\theta_i\}_{i=1}^m$, we obtain an operator $\mathcal{L}_\Theta : L^2(\mathbb{R}^2) \to L^2(\mathbb{R} \times [m])$:

$$\mathcal{L}_\Theta[\boldsymbol{Y}] := \tfrac{1}{\sqrt{m}} \left[\mathcal{L}_{\theta_1}[\boldsymbol{Y}], \ldots, \mathcal{L}_{\theta_m}[\boldsymbol{Y}] \right]. \tag{2.2}$$

Line scans. In reality, it is not possible to fabricate an infinitely sharp line probe, and hence our measurements do not correspond to ideal line projections, but rather their convolution with a point spread function ψ that models blurring along the scanning direction. In SECM, ψ is typically skewed, with a long tail in the sweeping direction. Accounting for this effect is important, if we wish to obtain accurate reconstructions in practice. In this more realistic model, our measurements become

$$\widetilde{\boldsymbol{R}} = \tfrac{1}{\sqrt{m}} [\psi * \mathcal{L}_{\theta_1}[\boldsymbol{Y}], \ldots, \psi * \mathcal{L}_{\theta_m}[\boldsymbol{Y}]] =: \psi * \mathcal{L}_\Theta[\boldsymbol{Y}]. \tag{2.3}$$

This measurement consists of m functions $\psi * \mathcal{L}_{\theta_i}[\boldsymbol{Y}](t)$ of a single (real) variable t, which corresponds to the translation of the probe in the $\boldsymbol{u}_{\theta_i}^\perp$ direction. In practice, we do not measure this function at every t, but rather collect n equispaced samples, giving measurements $\boldsymbol{R}_i = \mathcal{S}\{\widetilde{\boldsymbol{R}}_i\} \in \mathbb{R}^n$ and $\boldsymbol{R} = [\boldsymbol{R}_1, \ldots, \boldsymbol{R}_m] \in \mathbb{R}^{n \times m}$. Our task is to understand when and how we can reconstruct the target image $\boldsymbol{Y}$ from these samples.

3 Promises and problems of line scans

3.1 Compressed sensing of line projections for highly localized image

As a proof of concept, we first show that the line probe can efficiently sense sparse images consisting of well-separated features:

Lemma 3.1. *Consider an image consists of $k \geq 2$ discs radius r. If the centers $\boldsymbol{w}_1, \ldots, \boldsymbol{w}_k$ are separated such that $\min_{i \neq j} \|\boldsymbol{w}_i - \boldsymbol{w}_j\|_2 > \frac{2}{C} k^2 r$, then three line scans with probe direction chosen independent uniformly at random suffice to recover the image with probability at least $1 - C$.*

Lemma 3.1 shows if we assume the sparse component of the image signal are small and separated discs; if the radius of the discs are sufficiently small, then, perhaps surprisingly, only three line projections are required to exactly reconstruct the image.

3.2 Reconstructability from line projections of localized image in practice

While the microscopic images are often sparse in spatial domain, they rarely satisfy the conditions of Lemma 3.1. In the following, we show that in practical application of line scans, when the image consists of multiple localized motifs, the performance of line measurements degrades as the ratio between the size of motifs and their separation increases.
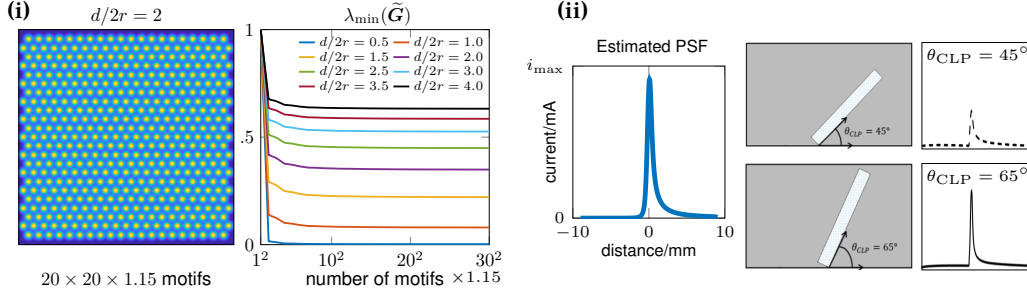
3

Figure 3: (i): Least eigenvalue of $\widetilde{G}$ with motifs on hexagonal lattice. We show an example image of motifs placed on the lattice locations (left), and calculate the least eigenvalue with varying number of motifs and distance-to-diameter ratio (right). **(ii)**: The point spread function of line probe is skewed in the sweeping direction. We show a close form PSF used for reconstruction (left); and software (LabVIEW) simulated PSF whose shape and intensity changes as the contacting angle varies (right).

Coherence of line projection of two localized motifs Inspired by CS, we study the conditioning of the line projection $\mathcal{L}_\Theta$ when it is restricted to an image with sparsely populated motifs $\boldsymbol{D} \in L^2(\mathbb{R}^2)$. Consider an image with two motifs located at different locations, and define a 2×2 Gram matrix $\boldsymbol{G}$ with its ij-th entries being *coherence* [36] between line projected signal of two motifs $\boldsymbol{D}$ with center at $\boldsymbol{w}_i$ and $\boldsymbol{w}_j$ respectively,

$$\boldsymbol{G}_{ij} = \left\langle \mathcal{L}_\Theta[\boldsymbol{D} * \boldsymbol{\delta}_{\boldsymbol{w}_i}], \, \mathcal{L}_\Theta[\boldsymbol{D} * \boldsymbol{\delta}_{\boldsymbol{w}_j}] \right\rangle. \tag{3.1}$$

If the off-diagonal entry $\boldsymbol{G}_{ij}$ is small in magnitude compared to the diagonal entries $\boldsymbol{G}_{ii}, \boldsymbol{G}_{jj}$, then it suffices to reconstruct the image exactly with efficient algorithm. Conversely, if $\boldsymbol{G}$ is ill-conditioned or even rank-deficient, then exact recovery will be impossible.

Lemma 3.2. *Let $\boldsymbol{D}$ be a two-dimensional Gaussian pdf with variance r and normalized in a sense that $\|\mathcal{L}_0[\boldsymbol{D}]\|_{L^2} = 1$. If θ is uniformly random, then the expectation of inner product between two line projected $\boldsymbol{D}$ at different locations $\boldsymbol{w}_i, \boldsymbol{w}_j$ is bounded by*

$$\left(1 - \frac{d^2}{8r^2}\right) \mathbf{1}_{d \le 2r} + \frac{r}{2d} \mathbf{1}_{d > 2r} \; \le \; \mathbb{E}_\theta \left\langle \mathcal{L}_\theta[\boldsymbol{D} * \boldsymbol{\delta}_{\boldsymbol{w}_i}], \, \mathcal{L}_\theta[\boldsymbol{D} * \boldsymbol{\delta}_{\boldsymbol{w}_j}] \right\rangle \; \le \; \frac{1}{\sqrt{1 + d^2/4r^2}}. \tag{3.2}$$

where $d = \|\boldsymbol{w}_i - \boldsymbol{w}_j\|_2$ and $\boldsymbol{\delta}_{\boldsymbol{w}}$ is the Dirac measure at $\boldsymbol{w}$.

Lemma 3.2 shows the coherence between line projections of two Gaussian of variance r and center distance d is dominated by the distance-to-diameter ratio $d/2r$. Because of the projection slice theorem, the matrix $\mathbb{E}_\theta \boldsymbol{G}$ is always positive definitive. However, its condition number greatly increases when the image is consists of highly overlapping local features. When the ratio is small, say $d/2r < 1$, in which the two projected motifs are overlapping, then $\mathbb{E}_\theta \boldsymbol{G}_{ij}$ will be close to one as with the diagonals, implies $\mathbb{E}_\theta \boldsymbol{G}$ become severely ill-conditioned even in the two-sparse case. Generally speaking, line scans are not CS-theoretical optimal sampling method for sparse recovery for image of superposing discs.

Injectivity of line projection of multiple motifs with minimum separation To extend the study of the coherence of matrix $\boldsymbol{G}$ to samples that contain $k > 2$ motifs $\boldsymbol{D}$. We first investigate a model configuration whose motif centers are allocated on a hexagonal lattice with edges of length d. It turns out that the smallest eigenvalue of an approximation $\boldsymbol{G}$ with respect to the locations $\{\boldsymbol{w}_1, \ldots, \boldsymbol{w}_k\}$ is largely determined by the distance-to-diameter ratio $d/2r$, and depends only weakly on the total number of motifs.

In Figure 3, we calculate the least eigenvalue of an approximation $\mathbb{E}_\theta \boldsymbol{G}$ with $\widetilde{G}$, where $\widetilde{G}_{ij} = (1 + \|\boldsymbol{w}_i - \boldsymbol{w}_j\|_2^2 / 4r^2)^{-1/2}$ is obtained from the upper bound in Lemma 3.2. We show that when these motifs are highly overlapping with distance-to-diameter ratio $d/2r = 0.5$, the least eigenvalue of $\widetilde{G}$ is very close to zero and the matrix is nearly rank-deficient; when the motifs are separated, say $d/2r \ge 1$, the least eigenvalue of $\widetilde{G}$ is steadily larger then zero and approaches one as the ratio $d/2r$ increases. Interestingly, in our experiments the least eigenvalue does not depend strongly on the number of motifs, suggesting that the distance-to-diameter ratio is the dominant factor for injectivity of line projections on motifs with hexagonal placement. Since the hexagonal configuration is the densest circle

4

packing on a plane, we suspect that $\lambda_{\min}(\mathbb{E}_\theta G)$ is also determined by the ratio $d/2r$ for every configurations satisfying the minimum separation property. This conjecture gains more ground when viewing this problem from the point source super-resolution perspective [35]. It is known that an image consisting of point measures $\boldsymbol{x} = \sum_i \alpha_i \boldsymbol{\delta}_{\boldsymbol{w}_i}$ can be stably recovered from its low frequency information (with frequency cutoff f_c) whenever the point sources have minimum separation $d > C/f_c$ for some constant C, regardless of the number of such point measures in $\boldsymbol{x}$. In our scenario, we will show that the expected line projection $\mathbb{E}_\theta \mathcal{L}_\theta^* \mathcal{L}_\theta$ is also a low-pass filter; and since the local features $\boldsymbol{D}$ is also often consists of low frequency components, our line projections $\mathcal{L}_\Theta[\boldsymbol{D} * \boldsymbol{X}]$ can be modeled as the low-pass measurements from sparse map $\boldsymbol{X}$, implying stable and efficient sparse reconstruction is possible as long as $\boldsymbol{X}$ is enough separated under infinitely many line measurements of all angles.

Lemma 3.3. *Suppose $\boldsymbol{D}$ is two-dimensional Gaussian of variance r with $\|\mathcal{L}_0[\boldsymbol{D}]\|_{L^2} = 1$ and $\boldsymbol{X}$ is finite summation of Dirac measure. If θ is uniformly random, then $\mathbb{E}_\theta \boldsymbol{D} * \mathcal{L}_\theta^* \mathcal{L}_\theta[\boldsymbol{D} * \boldsymbol{X}]$ is a lowpass filter $\mathcal{K}$ on $\boldsymbol{X}$ with cut-off frequency f_c satisfying*

$$f_c = \tfrac{1}{r} \cdot \min \left\{ 2r^2\varepsilon^{-1}, \sqrt{|\log(8r^2\varepsilon^{-1})|} + 0.2 \right\}, \tag{3.3}$$

in the sense that $\max_{\|\boldsymbol{\xi}\|_2 \geq f_c} |\mathcal{F}_2\{\mathcal{K}\}(\boldsymbol{\xi})| \leq \varepsilon$.

Lemma 3.3 shows when the radius of $\boldsymbol{D}$ is sufficiently large, then the cut-off frequency f_c is dominated by the cut-off frequency of $\boldsymbol{D}$, hence it is sufficient to recover $\boldsymbol{X}$ as long as the separation d satisfies $d > Cr$, which is also reflected from the observation of Figure 3. In cases with small (pointy) $\boldsymbol{D}$, the cut-off frequency is mainly determined by the low-pass property of line projection, which requires minimum separation $d > C\varepsilon/r$ for exact reconstruction.

3.3 Obstacles of image reconstruction from line scans

Besides the apparent nonideality of coherence of line scan measurements which is not CS theoretical optimal, this specific sampling method and its corresponding hardware limitations causes other practical nuisances during image reconstruction.

High coherence of line scans. To show the coherence is a cause for concern, consider the nonnegative Lasso

$$\min_{\boldsymbol{X} \geq 0} \lambda \|\boldsymbol{X}\|_1 + \tfrac{1}{2} \|\boldsymbol{A}[\boldsymbol{X}] - \boldsymbol{R}\|_2^2 \tag{3.4}$$

from observstion $\boldsymbol{R} = \boldsymbol{A}[\boldsymbol{X}_0]$ and linear, column normalized and coherent sampling method $\boldsymbol{A}$. Denote Ω as the support set of solution of (3.4), write $\boldsymbol{A}_\Omega$ as the submatrix of $\boldsymbol{A}$ restricted on columns of support Ω, the unique solution $\boldsymbol{X}$ of program (3.4) (provided if $\boldsymbol{A}_\Omega$ is injective) can be written as

$$\boldsymbol{X}_{ij} = \left[\boldsymbol{X}_{0ij} - \lambda(\boldsymbol{A}_\Omega^* \boldsymbol{A}_\Omega)^{-1}\boldsymbol{1}\right]_+ \ \ \boldsymbol{w}_{ij} \in \Omega; \qquad \boldsymbol{X}_{ij} = 0 \ \ \boldsymbol{w}_{ij} \notin \Omega. \tag{3.5}$$

When $\boldsymbol{A}$ is coherent, columns of $\boldsymbol{A}$ have large inner product, implies many entries of the matrix $\boldsymbol{A}_\Omega^* \boldsymbol{A}_\Omega$ have large, positive off-diagonal entries close to its diagonals. When the sparse penalty λ is large in (3.4), its solution will have incorrect relative magnitudes since $\boldsymbol{A}_\Omega^* \boldsymbol{A}_\Omega$ is not close to identity matrix as conventional CS measurements [37]. When λ is small, the solution of program will be highly sensitive to noise, occasionally leading to incorrect results.

Incomplete information of PSF of line scans. Another layer of complexity for CLP scans is the difficulty to correctly identify its PSF due to hardware limitations, especially when operating line scans in nanoscale. For instance in Figure 3 (right), we show if the contacting angle between the probe and the sample varies, the corresponding PSF changes drastically in both the peak magnitude and the shape. It turns out that even with seemingly small changes of probe condition, the corresponding PSF can be inevitably variated.

4 Reconstruction from line scans

In all following experiments, we consider a representative class of images $\boldsymbol{Y}$ characterized by superposing reactive species $\boldsymbol{D}$ at locations $\mathcal{W} = \{\boldsymbol{w}_1, \ldots, \boldsymbol{w}_{|\mathcal{W}|}\} \subset \mathbb{R}^2$ with intensities $\{\alpha_1, \ldots, \alpha_{|\mathcal{W}|}\} \subset \mathbb{R}_+$. Define the activation map $\boldsymbol{X}_0$ as sum of Dirac measure at $\mathcal{W}$, then $\boldsymbol{Y}$ can simply be written as convolution between $\boldsymbol{D}$ and $\boldsymbol{X}_0$:

$$\boldsymbol{Y} = \boldsymbol{D} * \boldsymbol{X}_0 = \sum_{j=1}^{|\mathcal{W}|} \alpha_j \boldsymbol{D} * \boldsymbol{\delta}_{\boldsymbol{w}_j}. \tag{4.1}$$

The image reconstruction problem is then cast as finding the best fitting sparse map $\widehat{\boldsymbol{X}}$ from line scans $\boldsymbol{R} = \mathcal{S}\{\boldsymbol{\Psi} * \mathcal{L}_\Theta[\boldsymbol{Y}]\}$, and the reconstructed image is simply $\boldsymbol{D} * \widehat{\boldsymbol{X}}$. Since all
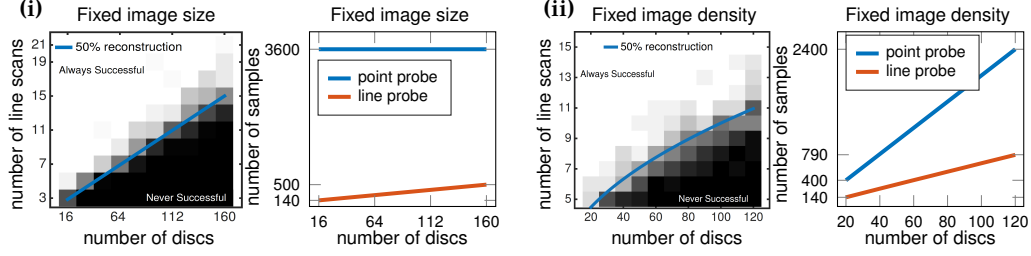
Figure 4: Phase transition [8] of fixed image size **(i)** and fixed density **(ii)** on support recovery with Lasso. In all experiments $d/2r \geq 1$ is ensured. Both of the phase transitions show the number of line scans required is almost linear proportional to the number of discs for exact reconstruction, and the scanning efficiency is better than point probe by 3-10 times.

associated operations on $\boldsymbol{X}_0$ (convolution with $\boldsymbol{D}, \boldsymbol{\psi}$ and line projection $\mathcal{L}_\Theta$) are all linear, this becomes a sparse estimation problem, which can be solved via the Lasso:

$$\min_{\boldsymbol{X} \geq 0} \lambda \sum_{ij} \boldsymbol{X}_{ij} + \tfrac{1}{2} \left\| \boldsymbol{R} - \mathcal{S}\{\boldsymbol{\psi} * \mathcal{L}_\Theta[\boldsymbol{D} * \boldsymbol{X}]\} \right\|_2^2. \tag{4.2}$$

4.1 Sparse recovery with Lasso from line projections

In light of Section 3.2, the measurement performance using infinitely many line scans is almost dependent only on the distance-to-diameter ratio of the local features. Since in practice, only finite number line scan is available, we want to study how many line scans will be sufficient for efficient and exact sparse image reconstruction. We do this by studying the performance of algorithm (4.2) while assuming the line scan are idealized where $\boldsymbol{\psi} = \boldsymbol{\delta}$.

Figure 4 shows the reconstruction performance from line scans with varying number of line scans (uniform randomly chosen angle) used and number of discs in the images $\boldsymbol{Y}$ (discs of radius r at random location satisfying $d/2r \geq 1$ via rejection sampling). Here, two experiment setting is presented: fixed area ($3 \times 3 \mathrm{mm}^2$, disc radius $50 \mu m$) and fixed density (20 discs/mm^2, disc radius $50 \mu m$). In the phase transition (PT) image, each pixel represents the average of 50 experiments; and in each experiment, given a random image $\boldsymbol{Y}$ line scans, if solving (4.2) correctly identify the support map of $\boldsymbol{Y}$, then the algorithm succeeds, and vise versa. It shows clear transition lines in both PT images, and the comparison of scanning time between line/point probes shows clear improvement of scanning efficiency.

Interestingly if we compare the result with CS theory, which asserts the number measurement of samples required is close to linear proportional to signal sparsity; here, though the line scans are not CS-optimal, both PT images exhibits similar phenomenon. When the image size is fixed, total number of samples m is proportional to the line scan count N, with PT transition line showing linear proportionality between number of line scans and discs $N \propto k$, gives $m \propto k$; on the other hand, when the image density is fixed, the number of samples m is proportional to $N \times \sqrt{k}$ while the transition line in PT is showing $N \propto \sqrt{k}$, again suggests linear proportionality between number of measurement and sparsity $m \propto N\sqrt{k} \propto k$.

In either case, line measurements are substantially more efficient than measurements with a point probe. Realizing this gain in practice requires us to modify the Lasso to cope with the following nonidealities: (i) line scans are coherent, (ii) the PSF $\boldsymbol{\psi}$ is typically only partially known, and (iii) naive approaches to computing with line scans are inefficient when the target resolution is large. Below, we show how to address these issues, and give a complete reconstruction algorithm.

4.2 Practical Reconstruction with Nonidealities

Fast computation of discrete line projection The line projection of an image $\boldsymbol{Y}$ in direction of angle θ is equivalent to the line projection at $0°$ of clockwise rotated $\boldsymbol{Y}$ by angle θ. This enables an efficient line projection computationally via fast image rotation with shear transform in Fourier domain [38] (see appendix); and more importantly, its adjoint (back projection) can be computed in a similarly explicit manner.

Reweighting Lasso for coherent measurements To cope with the coherence phenomenon, we adopt the reweighting scheme [39] by solving Lasso formulation (4.2) multiple times
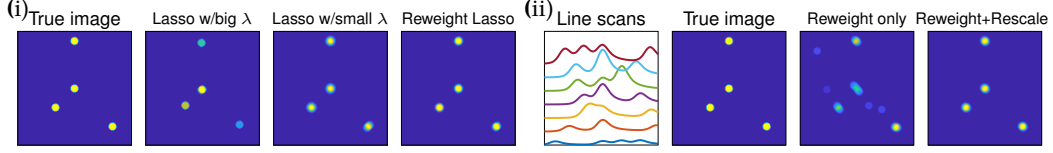
Figure 5: (i). To reconstruct the image (left) from 6 line scans with simulated PSF in Figure 3 using Lasso with large λ gives images of unbalanced magnitude (mid left) due to coherence; while using Lasso with small λ provides blurry image (mid right) due to the weakened sparsity regularizer. Reweighed Lasso (right) consistently generates good result. **(ii)**. We simulate a line scan with uneven magnitude (left) from image (mid left). Reweighting method (mid right) cannot identify the correct support; while the reweighting plus calibration method (right) approximately recovers the image.

while updating penalty variable $\boldsymbol{\lambda}$ in each iterate. At k-th iterate, the algorithm chooses the regularizer $\boldsymbol{\lambda}$ in (4.2) base on the previous outcome of lasso solution $\boldsymbol{X}^{(k)}$, where

$$\boldsymbol{\lambda}_{ij}^{(k)} \leftarrow C(\boldsymbol{X}_{ij}^{(k-1)} + \varepsilon)^{-1} \tag{4.3}$$

with ε being the machine precision constant and C being close to the smooth part in (4.2). The effect of reweighting method is two-fold: (i) it is a majorization-minimization algorithm of sparse regression using $\log$-norm as sparsity surrogate [39], hence, discovers sparse solution more effectively compares to the use of ℓ^1-norm in Lasso; and (ii) the sparsity surrogate in final stages of reweighting approaches ℓ^0-norm, by seeing $\frac{\boldsymbol{X}_{ij}^{(k+1)}}{\boldsymbol{X}_{ij}^{(k)}+\varepsilon} \approx 1$ if $\boldsymbol{X}_{ij}^{(k)} \neq 0$ as $k \to \infty$. As a result, in the final stages, problem (4.2) effectively turns into least squares, restricted to the support of $\boldsymbol{X}$, which produces a sparse solution with correct magnitude. Figure 5 (left) displays an example of reweighting scheme, showing better reconstruction result than vanilla Lasso.

Blind calibration for incomplete PSF information We can cope with incomplete information about the PSF by working with a parametric family of PSF's and optimizing the parameters at reconstruction time. Here, we allow the PSF to vary from scan to scan, writing $\boldsymbol{\psi}(\boldsymbol{p}_i)$ for the PSF for the i-th scan, with parameters $\boldsymbol{p}_i$. We optimize both the parameters $\boldsymbol{p}_1 \ldots \boldsymbol{p}_m$ and the sparse map $\boldsymbol{X}$ via alternating minimization. Figure 5 (right) exhibits a simulated example in which the PSF of line scans has unbalanced magnitudes due to the variation of probe scanning angle (Figure 3), suggests incorporating calibration scheme achieves successful reconstruction while non-calibration method falls short.

4.3 Image reconstruction algorithm from line scans

Finally we formally state the complete algorithm (see appendix) for reconstruction of SECM image from its line scans. The algorithm solves multiple iterations of

$$\min_{\boldsymbol{X} \geq 0, \boldsymbol{p} \in \mathcal{P}} \sum_{ij} \boldsymbol{\lambda}_{ij}^{(k)} \boldsymbol{X}_{ij} + \sum_{i=1}^{m} \frac{1}{2} \|\mathcal{S}\{\boldsymbol{\psi}(\boldsymbol{p}_i) * \mathcal{L}_{\theta_i}[\boldsymbol{D} * \boldsymbol{X}]\} - \boldsymbol{R}_i\|_2^2. \tag{4.4}$$

while updating the penalty variable $\boldsymbol{\lambda}^{(k)}$ in each iterate base on (4.3) with $C \approx \frac{1}{2}\|\mathcal{S}\{\boldsymbol{\psi} * \mathcal{L}_\Theta[\boldsymbol{D} * \boldsymbol{X}^{(k-1)}]\} - \boldsymbol{R}\|_2^2$. To solve a single iterate of (4.4), the algorithm utilize an accelerated alternating minimization method specifically for nonsmooth, nonconvex objectives (iPalm [40], see appendix). We choose the step size for this method by backtracking since (4.4) can be highly non-smooth locally.

5 Real data experiments

Figure 6-(i) compares the reconstruction result (10μm per pixel) between the line probe and point probe scans on a simplistic three disc samples (75μm radius, platinum). Here, the point probe tip diameter and the line probe edge thickness are equivalent ($\approx 20\mu$m), and the probe moving speed (100ms), the sampling period (10μm), and the probe end material (platinum) are identical as well. Four images are shown here, including the optical closeup image for the three discs, the line scans, and the reconstruction image of either point probe or the line probe. In the optical image, the straight arrow represents the probe sweeping direction, and the angular arrow states sample rotation direction (clockwise) with angle θ_s. In the reconstructed images, the black circles indicated the ground truth size and location of the discs derived from the optical image. The reconstruction algorithm is setup
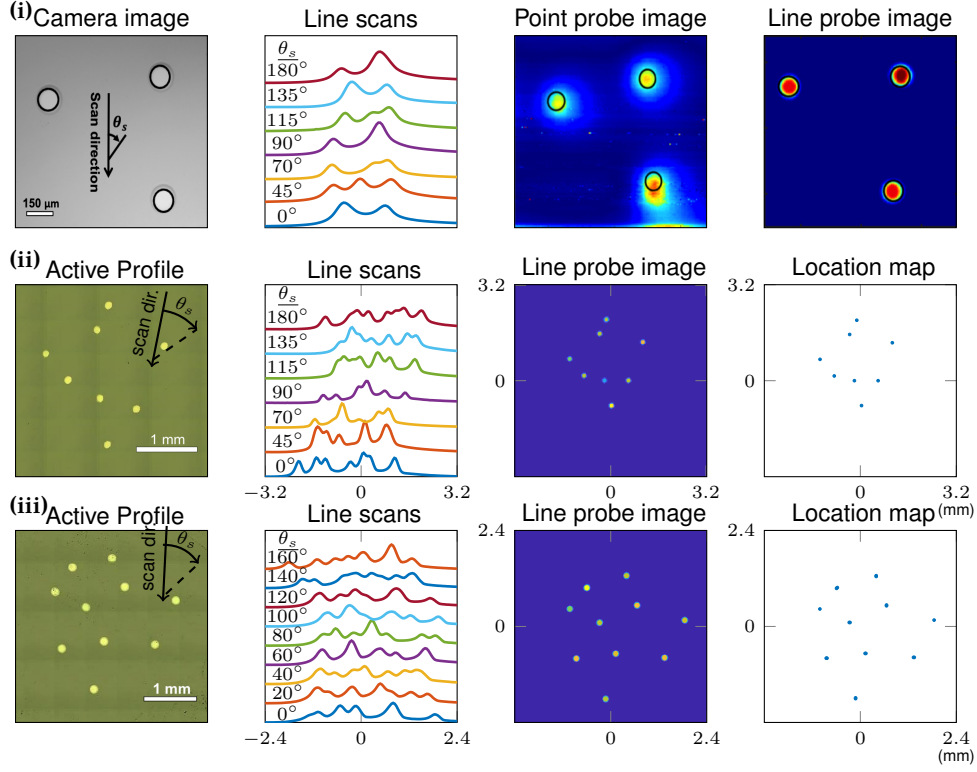
Figure 6: (i). Real data experiments on 3 platinum discs [41], the black circles in the microscopic images are derived from the disc location in camera image. **(ii)-(iii)**. Real data experiments of 8, 10 platinum discs, in which the location map is also the result of line scan reconstruction.

with 6 reweighting iterations, where each iterates runs 50 iterates of iPalm. We can see the reconstruction from point probe exhibits distortion in image due to the skewness of probe PSF along its proceeding direction during raster scans; while the image of line scan reconstruction presents three circular features with its size and locations are agreeing with the ground truth.

In Figure 6-(ii)-(iii), we reconstruct the image (20μm per pixel) of samples consist of platinum discs arranged in a more complicating configuration. Two sets of the experiment are presented here, which are the samples consist of 8 or 10 discs, while the disc diameter/image resolution/probe dimension/sampling period/algorithm iterations are all identical to the three discs case. We demonstrate both of the resulting reconstructed image and the location map defined by $\mathbf{1}_{\left\{\boldsymbol{X}_{ij} \geq 0.5 \|\boldsymbol{X}\|_{\infty}\right\}}$ at (i, j)-th entry. For these more complicated images, our algorithm are still able correctly identify the location and shape of the platinum discs. The corresponding location maps $\boldsymbol{X}$ are also estimated with reasonable accuracy.

6   Summary & Discussion

This paper describes issues, both theoretical and practical, that arise in reconstructing images from a new scanning probe microscopy technique, which has the potential to image sparsely populated samples much more efficiently than conventional approaches. There are many directions for future work. Our focus here has been on SECM, but the approach and technical results here are applicable to other scanning probe microscopy modalities, and are potentially applicable to other modalities such as CT that image based on projections. Motivated by materials science applications, our reconstruction approach focuses on images consisting of localized features; in other areas, different signal models may be approach. Unlike many other imaging modalities, in SPM the design of probe topography (i.e. the sampling pattern) is not limited to a straight line, therefore it is possible to adopt various different probe design accommodate different signal structures. Finally, obtaining sharp estimates of the required number of line scans is an interesting question for future theoretical work.

8

References

[1] R. Wiesendanger and W. Roland, *Scanning probe microscopy and spectroscopy: methods and applications*. Cambridge university press, 1994.

[2] D. L. Donoho *et al.*, "Compressed sensing," *IEEE Transactions on information theory*, vol. 52, no. 4, pp. 1289–1306, 2006.

[3] E. J. Candès and M. B. Wakin, "An introduction to compressive sampling [a sensing/sampling paradigm that goes against the common knowledge in data acquisition]," *IEEE signal processing magazine*, vol. 25, no. 2, pp. 21–30, 2008.

[4] S. Foucart and H. Rauhut, "A mathematical introduction to compressive sensing," *Bull. Am. Math*, vol. 54, pp. 151–165, 2017.

[5] M. Lustig, D. L. Donoho, J. M. Santos, and J. M. Pauly, "Compressed sensing mri," *IEEE signal processing magazine*, vol. 25, no. 2, p. 72, 2008.

[6] V. Studer, J. Bobin, M. Chahid, H. S. Mousavi, E. Candes, and M. Dahan, "Compressive fluorescence microscopy for biological and hyperspectral imaging," *Proceedings of the National Academy of Sciences*, vol. 109, no. 26, pp. E1679–E1687, 2012.

[7] A. Veeraraghavan, D. Reddy, and R. Raskar, "Coded strobing photography: Compressive sensing of high speed periodic videos," *IEEE Transactions on Pattern Analysis and Machine Intelligence*, vol. 33, no. 4, pp. 671–686, 2011.

[8] G. D. O'Neil, H.-W. Kuo, D. N. Lomax, J. Wright, and D. V. Esposito, "Scanning line probe microscopy: Beyond the point probe," *Analytical chemistry*, vol. 90, no. 19, pp. 11 531–11 537, 2018.

[9] A. J. Bard, L. R. Faulkner, J. Leddy, and C. G. Zoski, *Electrochemical methods: fundamentals and applications*. Wiley New York, 1980, vol. 2.

[10] A. J. Bard, F.-R. F. Fan, D. T. Pierce, P. R. Unwin, D. O. Wipf, and F. Zhou, "Chemical imaging of surfaces with the scanning electrochemical microscope," *Science*, vol. 254, no. 5028, pp. 68–74, 1991.

[11] G. N. Hounsfield, "Computerized transverse axial scanning (tomography): Part 1. description of system," *The British journal of radiology*, vol. 46, no. 552, pp. 1016–1022, 1973.

[12] A. C. Kak, "Computerized tomography with x-ray, emission, and ultrasound sources," *Proceedings of the IEEE*, vol. 67, no. 9, pp. 1245–1272, 1979.

[13] G. T. Herman, *Fundamentals of computerized tomography: image reconstruction from projections*. Springer Science & Business Media, 2009.

[14] S. L. Wellington, H. J. Vinegar *et al.*, "X-ray computerized tomography," *Journal of Petroleum Technology*, vol. 39, no. 08, pp. 885–898, 1987.

[15] N. Duric, P. Littrup, A. Babkin, D. Chambers, S. Azevedo, A. Kalinin, R. Pevzner, M. Tokarev, E. Holsapple, O. Rama *et al.*, "Development of ultrasound tomography for breast imaging: Technical assessment," *Medical Physics*, vol. 32, no. 5, pp. 1375–1386, 2005.

[16] J. Frank, *Electron tomography*. Springer, 1992.

[17] J. Nuyts, B. De Man, P. Dupont, M. Defrise, P. Suetens, and L. Mortelmans, "Iterative reconstruction for helical ct: a simulation study," *Physics in Medicine & Biology*, vol. 43, no. 4, p. 729, 1998.

[18] L. A. Shepp and B. F. Logan, "The fourier reconstruction of a head section," *IEEE Transactions on nuclear science*, vol. 21, no. 3, pp. 21–43, 1974.

[19] G.-H. Chen, J. Tang, and S. Leng, "Prior image constrained compressed sensing (piccs): a method to accurately reconstruct dynamic ct images from highly undersampled projection data sets," *Medical physics*, vol. 35, no. 2, pp. 660–663, 2008.

[20] K. Malczewski, "Pet image reconstruction using compressed sensing," in *2013 Signal Processing: Algorithms, Architectures, Arrangements, and Applications (SPA)*. IEEE, 2013, pp. 176–181.

[21] B. Goris, S. Bals, W. Van den Broek, E. Carbó-Argibay, S. Gómez-Graña, L. M. Liz-Marzán, and G. Van Tendeloo, "Atomic-scale determination of surface facets in gold nanorods," *Nature materials*, vol. 11, no. 11, p. 930, 2012.

[22] Z. Saghi, D. J. Holland, R. Leary, A. Falqui, G. Bertoni, A. J. Sederman, L. F. Gladden, and P. A. Midgley, "Three-dimensional morphology of iron oxide nanoparticles with reactive concave surfaces. a compressed sensing-electron tomography (cs-et) approach," *Nano letters*, vol. 11, no. 11, pp. 4666–4673, 2011.

[23] R. Leary, Z. Saghi, P. A. Midgley, and D. J. Holland, "Compressed sensing electron tomography," *Ultramicroscopy*, vol. 131, pp. 70–91, 2013.

[24] L. Donati, M. Nilchian, S. Trépout, C. Messaoudi, S. Marco, and M. Unser, "Compressed sensing for stem tomography," *Ultramicroscopy*, vol. 179, pp. 47–56, 2017.

[25] P. Binev, W. Dahmen, R. DeVore, P. Lamby, D. Savu, and R. Sharpley, "Compressed sensing and electron microscopy," in *Modeling Nanoscale Imaging in Electron Microscopy*. Springer, 2012, pp. 73–126.

[26] O. Nicoletti, F. de La Peña, R. K. Leary, D. J. Holland, C. Ducati, and P. A. Midgley, "Three-dimensional imaging of localized surface plasmon resonances of metal nanoparticles," *Nature*, vol. 502, no. 7469, p. 80, 2013.

[27] M. E. Davis, J. E. Zuckerman, C. H. J. Choi, D. Seligson, A. Tolcher, C. A. Alabi, Y. Yen, J. D. Heidel, and A. Ribas, "Evidence of rnai in humans from systemically administered sirna via targeted nanoparticles," *Nature*, vol. 464, no. 7291, p. 1067, 2010.

[28] C. A. S. Batista, R. G. Larson, and N. A. Kotov, "Nonadditivity of nanoparticle interactions," *Science*, vol. 350, no. 6257, p. 1242477, 2015.

[29] S. C. Cheung, J. Y. Shin, Y. Lau, Z. Chen, J. Sun, Y. Zhang, J. N. Wright, and A. N. Pasupathy, "Dictionary learning in fourier transform scanning tunneling spectroscopy," *arXiv preprint arXiv:1807.10752*, 2018.

[30] J. Radon, "1.1 über die bestimmung von funktionen durch ihre integralwerte längs gewisser mannigfaltigkeiten," *Classic papers in modern diagnostic radiology*, vol. 5, p. 21, 2005.

[31] A. M. Cormack, "Representation of a function by its line integrals, with some radiological applications," *Journal of applied physics*, vol. 34, no. 9, pp. 2722–2727, 1963.

[32] F. Natterer, *The Mathematics of Computerized Tomography*. Philadelphia, PA, USA: Society for Industrial and Applied Mathematics, 2001.

[33] S. Helgason, *Integral geometry and Radon transforms*. Springer Science & Business Media, 2010.

[34] S. Farsiu, D. Robinson, M. Elad, and P. Milanfar, "Advances and challenges in super-resolution," *International Journal of Imaging Systems and Technology*, vol. 14, no. 2, pp. 47–57, 2004.

[35] E. J. Candès and C. Fernandez-Granda, "Towards a mathematical theory of super-resolution," *Communications on Pure and Applied Mathematics*, vol. 67, no. 6, pp. 906–956, 2014.

[36] D. L. Donoho, M. Elad, and V. N. Temlyakov, "Stable recovery of sparse overcomplete representations in the presence of noise," *IEEE Transactions on information theory*, vol. 52, no. 1, pp. 6–18, 2006.

[37] E. Candes and T. Tao, "Decoding by linear programming," *arXiv preprint math/0502327*, 2005.

[38] K. G. Larkin, M. A. Oldfield, and H. Klemm, "Fast fourier method for the accurate rotation of sampled images," *Optics communications*, vol. 139, no. 1-3, pp. 99–106, 1997.

[39] E. J. Candes, M. B. Wakin, and S. P. Boyd, "Enhancing sparsity by reweighted l1 minimization," *Journal of Fourier analysis and applications*, vol. 14, no. 5-6, pp. 877–905, 2008.

[40] T. Pock and S. Sabach, "Inertial proximal alternating linearized minimization (ipalm) for nonconvex and nonsmooth problems," *SIAM Journal on Imaging Sciences*, vol. 9, no. 4, pp. 1756–1787, 2016.

[41] A. E. Dorfi, H.-W. Kuo, V. Smirnova, J. Wright, and D. V. Esposito, "Design and operation of a scanning electrochemical microscope for imaging with continuous line probes," *Manuscript submitted under review*, 2019.